Monthly Notices of the ROYAL ASTRONOMICAL SOCIETY
MNRAS **522,** 2675–2682 (2023) https://doi.org/10.1093/mnras/stad1085
Advance Access publication 2023 April 13

Photometric variations from stellar activity as an age indicator for solar-twins

Geisa Ponte ,[1,2★] Diego Lorenzo-Oliveira ,[2★] Jorge Melendez,[2] Jhon Yana Galarza[1,3] and Adriana Valio [1★]

[1]*Centro de Rádio Astronomia e Astrofísica Mackenzie (CRAAM), Universidade Presbiteriana Mackenzie, Rua da Consolação 930, 01302-907, São Paulo, SP, Brazil*
[2]*Departamento de Astronomia, Instituto de Astronomia, Geofísica e Ciências Atmosféricas, Universidade de São Paulo, Rua do Matão 1226, 05508-090, São Paulo, SP, Brazil*
[3]*The Observatories of the Carnegie Institution for Science, 813 Santa Barbara Street, Pasadena, CA, 91101, USA*

Accepted 2023 April 5. Received 2023 April 3; in original form 2023 February 23

ABSTRACT

Stellar ages are elusive to measure, albeit being very important for understanding stellar evolution. We investigate the impact of photospheric activity on 2-min cadence light curves from the *TESS*/NASA mission of a selected sample of 30 solar-twins with well-determined ages. The photometric variability, $\mathcal{A}_{TESS}$, of the light curves due to rotational modulations by the presence of active regions was estimated and correlated with chromospheric activity (Ca II H&K lines from an extensive High Accuracy Radial velocity Planet Searcher (HARPS) at the European Southern Observatory (ESO) HARPS/ESO activity time series) and ages. Moreover, these results were compared with the total solar irradiance amplitude behaviour during the solar magnetic cycles 23 and 24, validating our findings for solar-twins. Our results show the photometric amplitude to be strongly correlated to the average level of chromospheric activity for the star sample. Also, we found a good correlation of $\mathcal{A}_{TESS}$ with stellar age (in Gyr) described by $\log t = +12.239 - 0.894 \log \mathcal{A}_{TESS}$. In conclusion, stellar photometric variability $\mathcal{A}_{TESS}$ may be used as a simple age diagnostic for solar-twins.

Key words: techniques: photometric – techniques: spectroscopic – stars: activity – stars: solar-type.

1 INTRODUCTION

The brightness variability of stars on the time-scale of days is often attributed to dark spots crossing the stellar surface as the star rotates. Stellar activity, known to be associated with the occurrence of spots, depends on the age of the star (Barnes 2007). Young stars tend to be much more active and this activity decreases as the star ages. Some studies suggest that the solar photometric variability is significantly lower than that of other stars with similar age and temperature as the Sun (Shapiro et al. 2013). Moreover, Reinhold et al. (2020) found that most stars with periods similar to solar values are more active than the Sun, probably due to strong selection bias that it is not possible to measure the period from stars with solar like activity levels. However, this is not the case for most stars. In Basri et al. (2022), the authors demonstrate that the non-periodic subset of the Kepler solar-type sample, which constitutes over half of the total sample, being the majority of stars with rotation periods comparable to the Sun, exhibits photometric variability that is similar to that of the Sun.

At the same time, Hall, Lockwood & Skiff (2007) and Hall et al. (2009) showed that the chromospheric and photometric variabilities of the solar-twin 18 Scorpii, the closest and brightest known solar-twin (Porto de Mello & da Silva 1997; Soubiran & Triaud 2004; Petit et al. 2008) are very similar to solar values. However, solar observations are most of the time aimed at the equatorial plane, demonstrating a slightly different behaviour if compared to a sample of stars observed in arbitrary directions (Schatten 1993; Radick et al. 1998; Vieira et al. 2012). These factors could affect the apparent variability of solar-type stars and interfere directly in the comparison of solar with stellar photometric and chromospheric data.

Solar-twins were initially predicted by Cayrel de Strobel et al. (1981) based on the hypothesis that there are stars with observable spectroscopic parameters identical to the Sun, and the first known solar-twin were discovered by Porto de Mello & da Silva (1997). Because their fundamental properties show a remarkable resemblance to the Sun, the study of solar-twins offers multiple perspectives and numerous applications. One of the most relevant application involves their utility as a reference for the properties of the Sun itself.

Similarly, it is crucial to remember that calculating precise stellar ages has been a very arduous task (Soderblom 2010; Bazot et al. 2018). Among the different methods, a frequently applied technique is the use of isochrones, whereas other indirect methods involve stellar rotation (Barnes 2007; Lorenzo-Oliveira et al. 2019, 2020), stellar chromospheric activity (Mamajek & Hillenbrand 2008; Lorenzo-Oliveira et al. 2016a, 2018; Lorenzo-Oliveira, Porto de Mello & Schiavon 2016b), asteroseismology (Ulrich 1986; Silva Aguirre et al. 2017), and chemical clocks (Nissen 2015; Spina et al. 2018). Stellar ages are relevant for the study of stellar and Galaxy

★ E-mail: adrivalio@gmail.com (AV); diegolorenzo.astro@gmail.com (DLO); geisaponte.astro@gmail.com (GP)

evolution and the understanding of planetary systems formation and evolution.

Our goal is to measure periodic variations in the amplitude of stellar light curves due to stellar rotation using *TESS* data. Then, correlate these activity amplitudes with the average chromospheric activity index of a sample of solar-twins aged 50 Myr to 8.5 Gyr.

In the following section, we detail the solar-twin sample and the systematic trends that had to be corrected in the data. Measurements of the activity indicators of the stars such as photometric variation amplitude and chromospheric activity level are described in Section 3. Their relationship with stellar age is estimated in Section 4. Finally, our results are discussed and the main conclusions are presented in Section 5.

2 THE *TESS* SOLAR-TWIN SAMPLE

The photometric flux of each star is obtained from the Simple Aperture Photometry (SAP), the flux, after adding the calibrated pixels within the ideal photometric *TESS* aperture. The *TESS* pipeline defines the selected pixels around each target, and there may be an excess due to contamination of nearby stars. Thus, we restricted our sample to the light curves with less than 1 per cent of photometric contamination from neighbouring stars (*CROWDSAP* ≥ 0.99), photometric magnitudes less than 18 (*TESSMAG* ≤ 18), and *combined differential photometric precision* (*CDPP2_0*) $\leq 50\,000$ ppm.

Using these criteria, the remaining sample of selected stars by sector varied between 4946 (sector 21) and 11 497 (sector 4), which corresponds to a fraction between 29 and 60 per cent of the total number of stars in each sector. Moreover, each star had only one light curve per sector. These stars comprised the systematic control sample from all available TESS Input Catalog (TIC) stars.

For the variability analysis, we selected 30 stars observed by *TESS* from all 13 sectors in the first year of activity (Southern hemisphere) and one from sector 14 (Northern hemisphere), previously characterized as solar-twins. The selection criteria for these objects was based solely on the fact that they were *TESS* target stars (TIC) and had their spectroscopic parameters determined from HARPS/ESO spectrograph observations.

The list of well-characterized solar-twins was taken from Lorenzo-Oliveira et al. (2018, 2019). As these are stars that have been spectroscopically monitored over several years, there is information on the presence of orbiting planets (Bedell et al. 2015; Meléndez et al. 2017), possible chemical anomalies (e.g. Gratton et al. 2021; Yana Galarza et al. 2021), age (Spina et al. 2018), chromospheric activity levels (Lorenzo-Oliveira et al. 2018), rotation (dos Santos et al. 2016; Lorenzo-Oliveira et al. 2019, 2020), and other precise atmospheric parameters. The sample excludes spectroscopic binaries and stars with any chemical, rotational, or magnetic anomaly. We also excluded from the sample visual binaries that could still fall within the *TESS* observation aperture. The list of the analysed solar-twins and stellar parameters are listed in Table 1.

3 ACTIVITY INDICATORS

Two indicators of stellar activity are considered here: (i) the photometric fluctuations of the *TESS* light curves and (ii) the chromospheric contribution of the Ca II H&K lines extracted from HARPS/ESO spectra. The latter observation yields indices of magnetic activity and evolutionary properties, such as stellar age, which are listed in Table 1, for the sample of 30 analysed solar-twins.

3.1 Photometric variability amplitude: $\mathcal{A}_{TESS}$

As the star rotates, features on its surface such as dark spots or bright faculae cause brightness modulations perceived in the light curve. The periodicity of this modulation depends on the rotation period of the star, whereas the amplitude of the variation is related to the quantities and characteristics of the spots/faculae. These properties are illustrated in Fig. 1.

Before the photometric variability can be calculated, however it is necessary to estimate the systematic noise in the light curves. This noise may be due to fluctuation (*jitter*) from *TESS* pointing, in addition to inherent instrumental limitations. To remove these systematic trends in the observed *TESS* light curve, we built a tool that is explained in Appendix A.

First, the raw photometric amplitude of stellar variability is estimated in a similar way as McQuillan, Aigrain & Roberts (2012) and Basri, Walkowicz & Reiners (2013), using the median, the lower, and upper flux level for each star. These are calculated from the cumulative distributions (50 per cent, 2.5 per cent, and 97.5 per cent percentiles) defined in equation (1):

$$a'_{TESS} = \frac{f'_{\mathrm{P}97.5} - f'_{\mathrm{P}2.5}}{2 f'_{\mathrm{P}50}}. \quad (1)$$

Next, we mapped the instrumental photometric amplitude response due to differences in the apparent magnitude of the stars observed by *TESS*, using the complete sample of each sector. As expected, we found an apparent trend in all observed sectors, shown in the envelope in Fig. 2 for sector 10. The pink solid line represents the average of the lower 1 per cent percentile of the sample. We used an individual exponential fit for each sector which provided a baseline amplitude due to the systematic loss of sensitivity for fainter stars. Then, this baseline amplitude was subtracted from the measured a'_{TESS} for the selected solar-twins observed by *TESS* in that sector, yielding A_{TESS}.

Then, the rotation amplitudes, A_{TESS}, derived from solar-twins *TESS* light curves were converted into surface stellar fluxes (erg cm^{-2} s^{-1}) through synthetic flux calibration using the Phoenix model of atmospheres (assuming [Fe/H]$_\odot$ and $\log(g) = 4.5$; Husser et al. 2013). In short, for a given θ ($\theta \equiv 5040/T_{\mathrm{eff}}$), the surface flux distribution $f_\lambda(\theta)$ is convolved with the *TESS* transmission function (T_λ) over its photometric band ($\Delta\lambda = \lambda_2 - \lambda_1$):

$$\mathcal{F}_{TESS}(\theta) = \frac{\int_{\lambda_1}^{\lambda_2} f_\lambda(\theta) T_\lambda \delta\lambda}{\int_{\lambda_1}^{\lambda_2} T_\lambda \delta\lambda}, \quad (2)$$

where $\mathcal{F}_{TESS}$ represents the theoretical absolute flux in units of erg cm^{-2} s^{-1}. We build a grid of theoretical fluxes for FGKM spectral types (covering T_{eff} range of 3000–6500 K, assuming solar metallicity) and then, we calibrated the flux measurements as a function of T_{eff} :

$$\log \mathcal{F}_{TESS} = 0.1564\,\theta^3 - 0.4644\,\theta^2 - 1.303\,\theta + 8.113. \quad (3)$$

This photometric calibration is valid between 3000 and 6500 K, which includes completely the interval of T_{eff} used for the stars analysed in this work ($T_{\mathrm{eff}} = 5600$–5900 K). The flux fitting error ($\sigma^{\mathrm{fit}}_{\mathcal{F}_{TESS}}$) is 0.003 dex, which corresponds to a fractional error of $\approx$0.01 per cent. The absolute surface flux due to rotational modulation of the stars is estimated as

$$\mathcal{A}_{TESS} = A_{TESS} \times \langle \mathcal{F} \rangle_{TESS}\,, \quad (4)$$

where $\langle \mathcal{F} \rangle_{TESS}$ is given by equation (3) from the values of T_{eff} listed in Table 1.

Table 1. Parameters of the solar-twins used in this work. The age values were compiled from Lorenzo-Oliveira et al. (2019) and the atmospheric parameters from Spina et al. (2018).

HIP	T_{mag}	T_{eff} (K)	[Fe/H] (dex)	log(g) (dex)	Age (Gyr)	Mass ($\mathrm{M}_{\odot}$)	$\log R'_{\mathrm{HK}}(T_{\mathrm{eff}})$ (dex)
5301	7.83	5723 ± 3	-0.074 ± 0.003	4.395 ± 0.011	$6.3^{+0.3}_{-0.3}$	0.96 ± 0.03	-5.08 ± 0.03
8507	8.25	5717 ± 3	-0.099 ± 0.003	4.460 ± 0.011	$4.9^{+0.3}_{-0.3}$	0.95 ± 0.03	-5.02 ± 0.03
9141	7.42	5730 ± 50	0.000 ± 0.010	4.470 ± 0.010	$0.05^{+0.01}_{-0.01}$	1.00 ± 0.05	-4.314 ± 0.019
9349	7.37	5818 ± 6	-0.006 ± 0.005	4.515 ± 0.011	$0.4^{+0.3}_{-0.4}$	1.03 ± 0.03	-4.64 ± 0.05
11 915	7.99	5769 ± 4	-0.067 ± 0.004	4.480 ± 0.011	$3.0^{+0.3}_{-0.4}$	0.99 ± 0.03	-4.94 ± 0.04
15 527	6.76	5779 ± 4	-0.064 ± 0.003	4.335 ± 0.011	$7.4^{+0.4}_{-0.4}$	0.99 ± 0.03	-4.999 ± 0.019
22 263	5.03	5870 ± 7	0.037 ± 0.006	4.535 ± 0.013	$0.2^{+0.4}_{-0.2}$	1.06 ± 0.03	-4.59 ± 0.03
29 525	5.85	5741 ± 9	-0.012 ± 0.007	4.520 ± 0.016	$0.6^{+0.3}_{-0.3}$	1.00 ± 0.02	-4.528 ± 0.023
30 476	6.06	5709 ± 4	-0.033 ± 0.003	4.280 ± 0.011	$8.6^{+0.3}_{-0.3}$	1.01 ± 0.03	-5.141 ± 0.017
30 502	8.04	5731 ± 4	-0.057 ± 0.004	4.400 ± 0.013	$6.7^{+0.3}_{-0.5}$	0.96 ± 0.03	-5.084 ± 0.014
30 503	5.77	5873 ± 18	0.070 ± 0.016	4.410 ± 0.040	$3.0^{+0.7}_{-1.4}$	1.08 ± 0.03	-4.96 ± 0.03
33 094	5.25	5629 ± 7	0.023 ± 0.005	4.110 ± 0.016	$8.7^{+0.3}_{-0.4}$	1.07 ± 0.03	-5.229 ± 0.013
36 515	6.06	5855 ± 12	-0.029 ± 0.009	4.555 ± 0.023	$0.6^{+0.3}_{-0.4}$	1.02 ± 0.03	-4.44 ± 0.03
43 297	6.82	5705 ± 4	0.082 ± 0.003	4.505 ± 0.009	$0.4^{+0.4}_{-0.4}$	1.03 ± 0.03	-4.69 ± 0.06
44 713	6.68	5759 ± 3	0.063 ± 0.004	4.280 ± 0.010	$7.1^{+0.3}_{-0.3}$	1.04 ± 0.02	-5.022 ± 0.029
49 756	6.93	5789 ± 3	0.023 ± 0.003	4.435 ± 0.009	$4.9^{+0.3}_{-0.3}$	1.00 ± 0.03	-5.058 ± 0.014
54 287	6.59	5714 ± 4	0.107 ± 0.004	4.340 ± 0.012	$6.1^{+0.3}_{-0.4}$	1.02 ± 0.03	-5.14 ± 0.01
68 468	8.74	5845 ± 5	0.071 ± 0.004	4.330 ± 0.013	$5.5^{+0.3}_{-0.3}$	1.07 ± 0.03	-5.106 ± 0.026
69 645	8.78	5751 ± 3	-0.026 ± 0.004	4.435 ± 0.010	$5.5^{+0.4}_{-1.1}$	0.97 ± 0.03	-5.06 ± 0.03
74 389	7.15	5845 ± 3	0.083 ± 0.003	4.440 ± 0.011	$2.7^{+0.3}_{-0.3}$	1.06 ± 0.03	-4.92 ± 0.03
89 650	8.33	5851 ± 3	-0.015 ± 0.003	4.415 ± 0.011	$4.1^{+0.4}_{-0.4}$	1.04 ± 0.03	-5.06 ± 0.03
96 160	8.06	5798 ± 4	-0.036 ± 0.003	4.480 ± 0.012	$2.8^{+0.4}_{-0.3}$	1.00 ± 0.03	-4.899 ± 0.029
102 040	5.86	5853 ± 4	-0.080 ± 0.003	4.480 ± 0.012	$2.7^{+0.3}_{-0.3}$	0.99 ± 0.02	-4.948 ± 0.026
102 152	8.54	5718 ± 4	-0.016 ± 0.003	4.325 ± 0.011	$8.1^{+0.3}_{-0.3}$	0.97 ± 0.03	-5.119 ± 0.026
105 184	6.19	5843 ± 6	0.003 ± 0.004	4.510 ± 0.011	$0.5^{+0.5}_{-0.5}$	1.04 ± 0.03	-4.70 ± 0.03
108 158	6.80	5675 ± 4	0.055 ± 0.003	4.285 ± 0.011	$7.6^{+0.5}_{-0.9}$	1.04 ± 0.04	-5.098 ± 0.013
109 821	5.45	5747 ± 4	-0.108 ± 0.004	4.310 ± 0.011	$8.3^{+0.4}_{-0.4}$	0.99 ± 0.03	-5.106 ± 0.013
114 328	8.12	5775 ± 4	-0.017 ± 0.004	4.360 ± 0.012	$6.5^{+0.6}_{-0.9}$	1.00 ± 0.03	-5.10 ± 0.03
114 615	8.99	5819 ± 5	-0.063 ± 0.004	4.510 ± 0.009	$1.1^{+0.5}_{-0.4}$	1.02 ± 0.04	-4.83 ± 0.03
115 577	6.95	5694 ± 4	0.013 ± 0.003	4.260 ± 0.010	$8.0^{+0.3}_{-0.3}$	1.04 ± 0.03	-5.170 ± 0.016

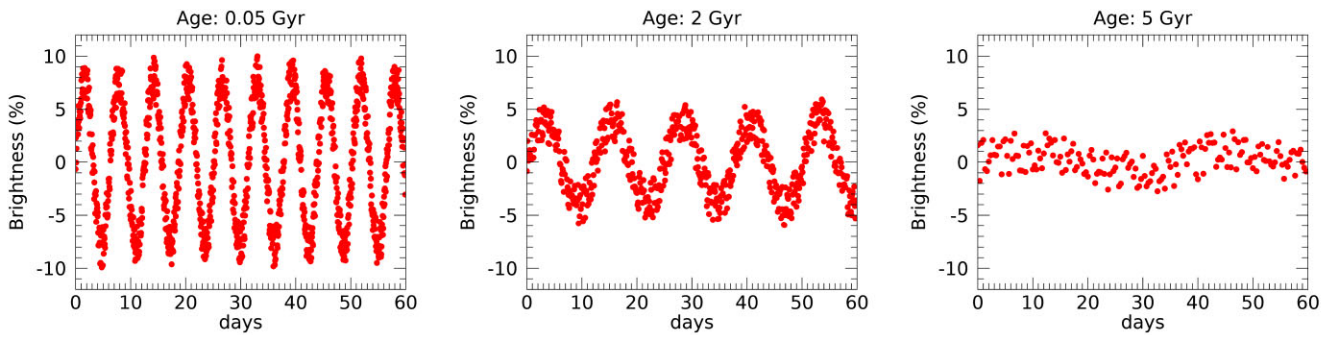

Figure 1. Illustration of the brightness variation of a star due to the spots size and rotation period of the star, which reflect the age of the star. Younger stars tend to have larger spots and brightness modulation of almost 10 per cent, which decreases as the star ages. Schematics of the stars light curve brightness variation are shown for stars of 50 Myr (left-hand panel), 2 Gyr (middle), and 5 Gyr (right-hand panel). It is worth mentioning that in these model light curves, any spot evolution on time-scales of the rotational period is not considered.

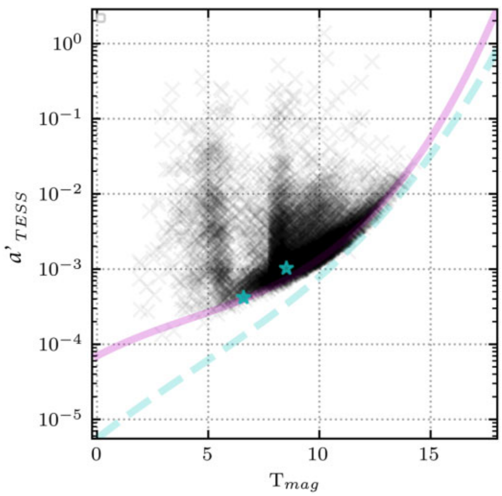

Figure 2. Photometric amplitude response as a function of the stars' visual magnitude observed in sector 10. The two solar-twins present in this sector are depicted by the cyan stars. The pink line shows the envelope of this sector and the amplitude trend dominated by noise. The dashed cyan line shows the amplitude detection limit due to photon noise.

3.2 Amplitude variability of the Sun

For comparison, we derive the amplitude modulation of the Sun's brightness due to solar photospheric activity. For that, the total solar irradiance (TSI) measured by the variability of solar irradiance and gravity oscillations (VIRGO; Andersen 1991) instrument aboard the *SOHO* satellite is used. First, the TSI needs to be converted before it can be compared directly to the brightness variability of other stars, which typically covers much narrower wavelength bands. Therefore, accurate estimates of the solar variability in the *TESS* passbands are made following Nèmec et al. (2020).

TESS observations are made in sectors of just 27 d each, thus the measured $\mathcal{A}_{TESS}$ may be smaller during a period of minimum stellar activity cycle when compared to a period of maximum activity of the star. However, the magnetic activity cycle of our sample of solar-twins have not been established yet, but the Sun may be used as a reference.

Since there are 22 yr of TSI data available, we investigate how the variability measurements are affected by the phase of the solar magnetic cycle. However, the Sun is a middle-aged star and the sample of solar-twins contemplates very young stars (of 50 Myr) to stars much older than the Sun (up to 8.5 Gyr). Therefore, the Sun will not necessarily provide the level of variability of the $\mathcal{A}_{TESS}$ for solar-twins with different ages, which may vary according to its intrinsic level of magnetic activity.

The amplitude variability measured for the Sun is denoted by $\log \mathcal{A}_{\odot,TESS}$ and measured from the TSI data in the same way as for the other stars, using equation (1). First the temporal resolution of the TSI data of 1 h is interpolated to match that of *TESS* of 2 min. Furthermore, the solar amplitude measured is multiplied by a factor of 0.939, because the variability of the flux in the *TESS* band is about 7 per cent lower than that of the TSI (see the conclusion, followed by fig. 4 and tables 1 and 2 of Nèmec et al. 2020).

To measure $\log \mathcal{A}_{\odot,TESS}$, we used TSI data for two solar activity cycles, 23 and 24, for a total of 22 yr. The solar variability, $\log \mathcal{A}_{\odot,TESS}$, was estimated every 27 d simulating *TESS* observations throughout 301 sectors, which are shown in Fig. 3. A histogram of all $\log \mathcal{A}_{\odot,TESS}$ is plotted in the top panel of Fig. 3, whereas the evolution of $\log \mathcal{A}_{\odot,TESS}$ in time for two solar activity cycles is shown in the middle panel of Fig. 3. The median of $\log \mathcal{A}_{\odot,TESS}$ measurements found was

$$\log \bar{\mathcal{A}}_{\odot,TESS} = 2.87^{+0.27}_{-0.4}. \quad (5)$$

The lower limit for the solar amplitude variability was estimated from the TSI uncertainty of $\sim$2.47 W m^{-2} and, as can be seen in the middle panel of Fig. 3, the photometric solar variability can be detected throughout the solar cycle due to the presence of active regions on the Sun.

In the bottom panel of Fig. 3, the calculated $\log \mathcal{A}_{\odot,TESS}$ (black curve) is overplotted on the observed TSI (magenta curve). As can be seen from the middle and bottom panels, the $\log \mathcal{A}_{\odot,TESS}$ roughly follows the solar cycle. There are some outliers, such as the maximum amplitude variation during the descent of solar cycle 23 near 3000 in JD-245000, when a group of very large active regions caused a decrease of 0.34 per cent in TSI. During the end of October and beginning of 2003, the Sun produced a few very energetic solar flares and coronal mass ejections, which became known as the Halloween events (Mannucci et al. 2005; Cid et al. 2015).

3.3 Chromospheric activity: $\log R'_{\rm HK}$

The average chromospheric activity, $\log R'_{\rm HK}$, for the stars in our sample is listed in the last column of Table 1 and was obtained from HARPS/ESO spectrograph observations (Lorenzo-Oliveira et al. 2019). The correlation between this average chromospheric activity with $\mathcal{A}_{TESS}$ from the sample of stars and the Sun is shown in the left-hand panel of Fig. 4. The Pearson correlation coefficient (ρ) between the two distributions is $\rho = 0.84 \pm 0.05$, with its respective p-value $= 2.7 \times 10^{-7}$, thus indicating that the probability that ρ is null, in this case is very low.

In Fig. 4, the coloured sidebar shows the distribution of the stars effective temperature, evidencing no apparent bias. The black Sun's symbol, $\odot$, represents the median of 301 amplitudes of log $\log \bar{\mathcal{A}}_{\odot,TESS}$ (see equation 5) measured every 27 d over 22 yr of TSI observations (see Section 3.2).

The results show that stars with larger photometric amplitude $\mathcal{A}_{TESS}$ are also the ones with larger $\log R'_{\rm HK}$, which is consistent and within what is expected for very active stars. Moreover, it has also been confirmed for the Sun, which falls within the observed correlation. This relation is well explained by the presence of a bigger number of magnetic structures on the stellar surface, which causes larger modulation of the stellar brightness (see Fig. 1).

We found that photometric variability is quite common for stars with high chromospheric activity, reinforcing the strong connection between chromospheric and photospheric activity. For inactive stars, a theoretical transition from photometric dominance between spots (younger stars) and faculae (older stars) is expected. According to recent work (e.g. Shapiro et al. 2020), this phenomenon must have occurred in the Sun at around $\sim$3 Gyr old, depending on the spectral region analysed. From the point of view of the chromospheric age–activity relation of solar-twins (Lorenzo-Oliveira et al. 2018), this age range corresponds to a chromospheric activity level of $\log R'_{\rm HK} \sim -4.9$, coinciding with the first non-detections of variability that we found in our work. Spots and faculae have distinct effects in the light curves, thus hindering the physical connection between amplitude measurements and photometric activity levels. Another point to emphasize is that spectroscopic measurements have greater sensitivity than photometric ones, even when considering the state of the art available photometric instrumentation, such as *TESS*.

The typical detection limit for $\log \mathcal{A}_{TESS}$ in our analysis is around $\sim$3, depending on the apparent magnitude of the star. For this

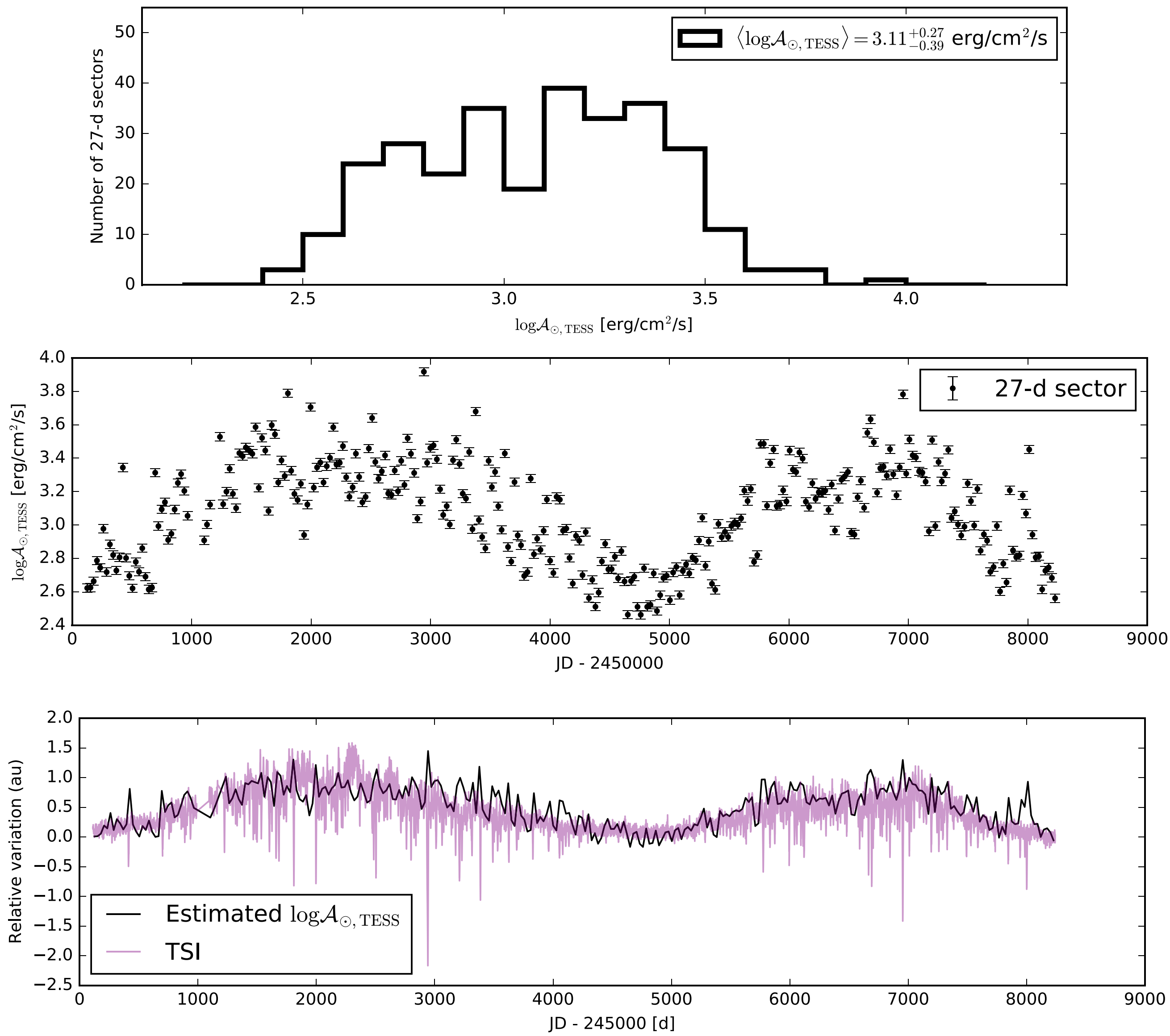

Figure 3. Top: Histogram of $\log \mathcal{A}_{\odot,\ TESS}$ measured for 301 hypothetical sectors of TSI observations during 22 yr. Middle: Temporal evolution of $\log \mathcal{A}_{\odot,\ TESS}$ throughout the solar activity cycles 23 and 24. Bottom: TSI observations (magenta curve) and $\log \mathcal{A}_{\odot,\ TESS}$ estimates (black curve) for solar activity cycles 23 and 24.

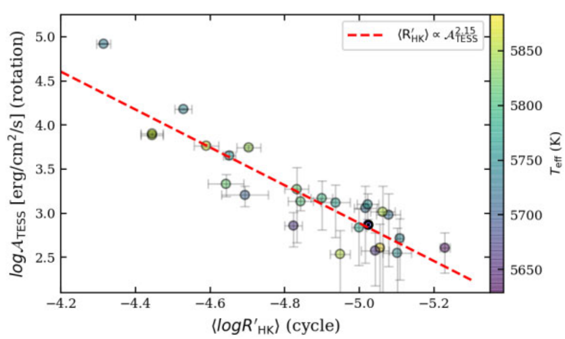

Figure 4. Correlation between the photometric index $\mathcal{A}_{TESS}$ and the chromospheric activity index $\log R'_{\mathrm{HK}}$. The black point, $\odot$, is the median of 301 amplitudes of $\log \mathcal{A}_{\odot,TESS}$ measured every 27 d over 22 yr of TSI observations. The red dashed line is a fit to the correlation given by equation (6).

reason, we have amplitude detection superimposed on non-detected amplitudes for the same range of stellar activity. This limit is due to the signal saturation of the photometric variability, which is already very low (e.g. older stars) and within the uncertainties. Besides, the *TESS* observation window (27 d) does not necessarily cover the entire rotational period of these stars (when only in one sector), as they rotate much slower.

Although the limitations stated above are relevant factors for our analysis, the strong correlation between photometric amplitudes and levels of chromospheric activities is evident for the stars considered here. Therefore, we use solar-twins with amplitude detection to fit the relationship between $\mathcal{A}_{TESS}$ and $\log R'_{\mathrm{HK}}$:

$$\log \mathcal{A}_{TESS} = \alpha + \beta \log R'_{\mathrm{HK}}(T_{\mathrm{eff}}), \quad (6)$$

which yield $\alpha = 13.9$ and $\beta = 2.15$, with typical errors of $\sim$0.2 dex. This power law, $\log R'_{\mathrm{HK}}(T_{\mathrm{eff}}) \propto \mathcal{A}^{2.15}_{TESS}$, is plotted in Fig. 4 as a red dashed line.

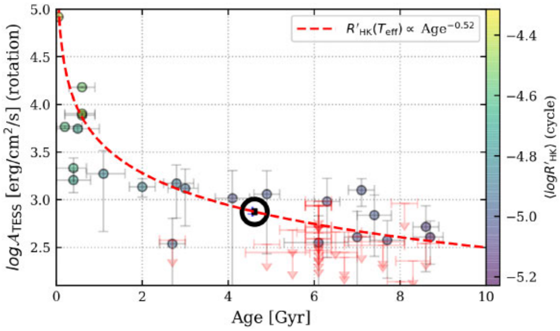

Figure 5. The evolution of $\mathcal{A}_{TESS}$ with age. The red dashed line is the forecast for the evolution of photometric amplitude (see equation 9). The black point referring to $\log \bar{\mathcal{A}}_{\odot,TESS}$, is the median of the amplitude values in the 301 'sectors' TSI measured over 22 yr.

The correlation between photometric and chromospheric variability may be understood as an evolution of the stellar dynamo. Inheriting angular momentum from the primordial molecular cloud, young stars have high activity and rotation rate. Over time, these stars lose angular momentum due to a magnetized wind, decreasing their rotation and magnetic activity level (illustrated in Fig. 1). This close relationship between the evolution of stellar rotation and activity level is the key for constructing stellar chronometers based on the amplitude of photometric variability. However, different activity features that depend on specific astrophysical conditions, may evolve faster/slower on different time-scales (Ribas et al. 2005). This seems to be the case of the photospheric activity measured by *TESS* light curves, which is dominated by the fraction of surface spot coverage. As an example, simultaneous measurements of solar activity features indicate that spots decay faster than facular coverage as a function of Ca II S-index activity (Shapiro et al. 2014). Hence, on secular time-scales, the steep dependence $\beta \sim 2$ found in this work also evidences a faster decrease of spot contribution on solar-twins. However, for distant stars unlike the Sun, the detected spot contribution emerges into basal instrumental noise levels at earlier evolutionary stages in comparison to the chromospheric counterparts, such as the Ca II lines. This result will be further discussed in Appendix B.

4 RELATIONSHIP OF $\mathcal{A}_{TESS}$ WITH AGE

In Fig. 5, the correlation between ages and $\mathcal{A}_{TESS}$ is shown for solar-twins and the Sun. The stellar ages were calculated using precise atmospheric parameters and *Gaia* DR2 parallax to obtain the best evolutionary trajectories. The coloured sidebar represents $\log R'_{HK}$ confirming the pattern in all three dimensions.

A decrease of the photometric amplitude with age is clearly seen in Fig. 5. Next, we combined the relationship of the photometric amplitude and chromospheric activity, given by equation (6), with the chromospheric age–activity relation derived from a previous study of a large sample of solar-twins by Lorenzo-Oliveira et al. (2018), to obtain a phenomenological relation between photometric amplitude and age. The Lorenzo-Oliveira et al. (2018) age–activity relationship is given by equation:

$$\log(t_{HK}) = \gamma + \delta \log R'_{HK}(T_{eff}), \tag{7}$$

where $\gamma = 0.0534$, $\delta = -1.92$, and t_{HK} is the age in years. By combining equations.(6) and (7), we can predict the evolution of photometric activity without a new calibration, avoiding propagating more free parameters. After isolating the term of interest that is the stellar age, assuming $t_{HK} \equiv t$, one obtains the stellar chronometer equation:

$$\log t = +12.239 - 0.894 \log \mathcal{A}_{TESS} \tag{8}$$

or, by isolating the activity term:

$$\log \mathcal{A}_{TESS} = +13.69 - 1.12 \log t, \tag{9}$$

where the typical age dispersion found is ±2.1 Gyr. Equation (9) is shown as the red dashed curve in Fig. 5. This relation should be interpreted as a prediction of the photometric amplitude decay with stellar age. In comparison to the Skumanich-like relation (activity $\propto t^n$, where $n \approx -0.5$), the equation (9) has a steeper decay of photometric variability with $n = -1.12$.

For comparison, we also plot the known values of the Sun as a black circle in Fig. 5. It is remarkable that the location of the Sun point, which was built using the TSI data, is exactly on top of the age forecast curve (in red). We can calculate the age of the Sun from the amplitude given by equation (8) $t_{\odot} = 4.5^{+5.1}_{-1.9}$ billion years, which is very consistent with the known solar age ($t_{\odot} = 4.6$ Gyr).

5 DISCUSSION AND CONCLUSIONS

We have analysed the photometric variability, $\mathcal{A}_{TESS}$, of 30 solar-twins using light curves from *TESS*. These results were correlated with the average chromospheric activity index $\log R'_{HK}$ and stellar ages to propose a potential new stellar age indicator. The measured photometric variability, detected on *TESS* light curves, is thought to be due to the rotational modulation of active regions, especially the presence of starspots and faculae on the stellar surface (see Fig. 1). In the process, we built a new tool that optimizes the removal of *TESS* instrumental systematics, so as to maximize the amplitude of photometric variability (see Appendix A).

Our results have shown that the photometric amplitudes of the solar-twins in our sample are strongly correlated with levels of chromospheric activity as well as with age. This result agrees with the banana-like trend found by Lorenzo-Oliveira et al. (2018), who established a robust relationship between age and chromospheric activity of solar-twins. Finally, we understand that $\mathcal{A}_{TESS}$ can be used as a stellar chronometer for solar-twins observed by *TESS*, summarized in equation (8).

There are some possible degeneracies that may affect our results. One of them is the inclination angle of the stellar spin-axis along the observer line of sight. Although the photometric variability and the estimate of the stellar rotation period depend strongly on the inclination of a star (Nèmec et al. 2020), the chromospheric activity shows a much weaker dependence (Shapiro et al. 2014). In particular, if a star is observed with a relatively low inclination angle (i.e. almost pole-on), its rotational variability would be significantly reduced, and perhaps classified as non-periodic, hence its calculated $\mathcal{A}_{TESS}$ would be much smaller than expected for its level of chromospheric activity. Still, the trend and the observed age refers to the behaviour observed by dos Santos et al. (2016), when studying the evolution of the rotational velocity projected along the line of sight of a sample of solar-twins.

Moreover, stars present cyclic magnetic activity with periodicity of years. Thus, the phase of the cycle when the star is observed by *TESS* may also affect the level of $\mathcal{A}_{TESS}$ measured for the same age or average activity level. If the star is observed at a time of maximum activity cycle, its light curve would naturally tend to show a larger $\mathcal{A}_{TESS}$ than if it had been observed at a time of minimum of the activity cycle. This behaviour was studied in detail for the Sun, and corroborated the influence of the cycle phase on the activity index.

Furthermore, very young and extremely active stars may present a saturation of active regions on their photosphere. Such stars would have a surface so crowded with spots that no rotation modulation in their light curve would be identified. In these extremely young and active stars, the $\mathcal{A}_{TESS}$ may be underestimated or saturated, due to the small contrast between regions without spots (higher brightness) or with spots (lower brightness). Also, differences in spot size and intensity can cause degeneracy in the determination of $\mathcal{A}_{TESS}$. For example, a star covered by weaker (small contrast) but very large spots would yield the same $\mathcal{A}_{TESS}$ value as another star with smaller, but darker spots. This is because the light curve brightness deficit due to large area of lighter spots can be similar to a small very dark area.

The age of a star is difficult to estimate, albeit being a very important parameter in stellar and planetary system evolution. Here, we proposed a very simple method to estimate the age of a star which appears to work for stars with a broad range of ages, from young (50 Myr) to stars older than our Sun (8.5 Gyr). Hopefully, this easy to use stellar chronometer can be applied to a broader sample of stars.

ACKNOWLEDGEMENTS

GP is grateful to the tenacious Brazilian workers and taxpayers, whose effort enabled the existence of this project, moreover she acknowledges the support from Coordination of Superior Level Staff Improvement (CAPES), São Paulo Research Foundation (FAPESP), and MackPesquisa fundings. DLO, JM, and AV thank the support from FAPESP (2016/20667-8, 2018/04055-8). JYG acknowledges the support from a Carnegie Fellowship and National Council for Scientific and Technological Development (CNPq) (166042/2020-0). This research was possible thanks to *TESS* ID programmes G011208 for Cycle 1 and G022106 for Cycle 2.

DATA AVAILABILITY

The data from the *TESS*/NASA underlying this article are available from the *Mikulsky Archive for Space Telescopes* page at https://archive.stsci.edu/missions-and-data/tess, as well as the TSI solar time series can be downloaded from the Virgo/*SOHO* webpage https://www.pmodwrc.ch/en/research-development/space/soho/#SOHO-VIRGO.

REFERENCES

Andersen B. N., 1991, Adv. Space Res., 11, 93
Barnes S. A., 2007, ApJ, 669, 1167
Basri G., Walkowicz L. M., Reiners A., 2013, ApJ, 769, 37
Basri G., Streichenberger T., McWard C., Edmond Lawrence I., Tan J., Lee M., Melton T., 2022, ApJ, 924, 31
Bazot M., Creevey O., Christensen-Dalsgaard J., Meléndez J., 2018, A&A, 619, A172
Bedell M. et al., 2015, A&A, 581, A34
Cayrel de Strobel G., Knowles N., Hernandez G., Bentolila C., 1981, A&A, 94, 1
Cid C., Saiz E., Guerrero A., Palacios J., Cerrato Y., 2015, J. Space Weather Space Clim., 5, A16
dos Santos L. A. et al., 2016, A&A, 592, A156
Gratton R. et al., 2021, A&A, 646, A61
Hall J. C., Lockwood G. W., Skiff B. A., 2007, AJ, 133, 862
Hall J. C., Henry G. W., Lockwood G. W., Skiff B. A., Saar S. H., 2009, AJ, 138, 312
Husser T.-O., Wende-von Berg S., Dreizler S., Homeier D., Reiners A., Barman T., Hauschildt P. H., 2013, A&A, 553, A6
Lorenzo-Oliveira D., Porto de Mello G. F., Dutra-Ferreira L., Ribas I., 2016a, A&A, 595, A11
Lorenzo-Oliveira D., Porto de Mello G. F., Schiavon R. P., 2016b, A&A, 594, L3A
Lorenzo-Oliveira D. et al., 2018, A&A, 619, A73
Lorenzo-Oliveira D. et al., 2019, MNRAS, 485, L68
Lorenzo-Oliveira D., Meléndez J., Ponte G., Galarza J. Y., 2020, MNRAS, 495, L61
McQuillan A., Aigrain S., Roberts S., 2012, A&A, 539, A137
Mamajek E. E., Hillenbrand L. A., 2008, ApJ, 687, 1264
Mannucci A. J. et al., 2005, Geophys. Res. Lett., 32, L12S02
Meléndez J. et al., 2017, A&A, 597, A34
Morris B. M., 2020, ApJ, 893, 67
Nèmec N.-E., Işık E., Shapiro A. I., Solanki S. K., Krivova N. A., Unruh Y., 2020, A&A, 638, A56
Nissen P. E., 2015, A&A, 579, A52
Petit P. et al., 2008, MNRAS, 388, 80
Porto de Mello G. F., da Silva L., 1997, ApJ, 482, L89
Radick R. R., Lockwood G. W., Skiff B. A., Baliunas S. L., 1998, ApJS, 118, 239
Reinhold T., Shapiro A. I., Solanki S. K., Montet B. T., Krivova N. A., Cameron R. H., Amazo-Gómez E. M., 2020, Science, 368, 518
Ribas I., Guinan E. F., Güdel M., Audard M., 2005, ApJ, 622, 680
Schatten K. H., 1993, J. Geophys. Res., 98, 18907
Shapiro A. I., Schmutz W., Cessateur G., Rozanov E., 2013, A&A, 552, A114
Shapiro A. I., Solanki S. K., Krivova N. A., Schmutz W. K., Ball W. T., Knaack R., Rozanov E. V., Unruh Y. C., 2014, A&A, 569, A38
Shapiro A. V., Shapiro A. I., Gizon L., Krivova N. A., Solanki S. K., 2020, A&A, 636, A83
Silva Aguirre V. et al., 2017, ApJ, 835, 173
Soderblom D. R., 2010, ARA&A, 48, 581
Soubiran C., Triaud A., 2004, A&A, 418, 1089
Spina L. et al., 2018, MNRAS, 474, 2580
Ulrich R. K., 1986, ApJ, 306, L37
Vieira L. E. A., Norton A., Dudok de Wit T., Kretzschmar M., Schmidt G. A., Cheung M. C. M., 2012, Geophys. Res. Lett., 39, L16104
Yana Galarza J., Meléndez J., Karakas A. I., Asplund M., Lorenzo-Oliveira D., 2021, MNRAS, 502, L104

APPENDIX A: REMOVAL OF SYSTEMATIC TRENDS IN EACH *TESS* SECTOR

Our main objective was to build a tool that optimizes the removal of instrumental systematics from the *TESS* mission, maximizing the calculation of the amplitude of photometric variability due to the passage of active regions on the stellar surface. Since *TESS* is a spacecraft, the pointing of the data acquisition cameras provides an extra systematic error compared to ground-based telescopes. In addition to this, other sources of noise include the photon counts of stars and also of the background (zodiacal light, weak stars, and unresolved objects that may appear in the background), CCD dark current, even if very small, in addition to readout noise and additional systematics errors that cannot be corrected by any removal method. The most important source of systematic noise arises from variations in random pointing caused by the spacecraft jitter.

The variability due to long-term pointing across the *TESS*' sectors can affect the overall observed stellar flux. For this, we use the PCA method, or principal component analysis. PCA is a mathematical procedure that uses vectors orthogonalization to convert a set of possibly correlated variables in a set of linearly independent variables, called principal components. The idea here is to find the components responsible for the larger variations of the light curves of the control star sample. Thus, we identify these components responsible for the instrumental systematics, that is, which do not result from stellar physical processes.

For this, we used the reduction of linear dimensionality using the singular value decomposition to project in a smaller dimensional space. Before determining the main components, it was necessary to perform some intermediate steps. In each sector, we define a grid of i constant steps in time for all light curves. We ensured that for missing cadences, the flux value $f_i^{\rm SAP}$ was defined from the linear interpolation between the neighbouring cadences ($f_{i-1}^{\rm SAP}$ and $f_{i+1}^{\rm SAP}$). To make the dimensionality reduction procedure independent of the scale adopted, we standardize the measurements of $f^{\rm SAP}$, thus ensuring that flux variations in each light curve were between -2 and $+2$.

We built a matrix $X^{\rm SAP}$ defined by the standardized matrix of the values $f_{ij}^{\rm SAP}$ containing all the sector light curves. Each cadence t_i is given by the matrix lines, while $f_j^{\rm SAP}$ from each j observation compose the columns of $X^{\rm SAP}$. To derive the matrix containing the main systematics in the light curve emsemble, $X^{\rm PCA}$, we use the SVD matrix decomposition in $X^{\rm SAP}$, to estimate the respective eigenvalues and eigenvectors. These elements provide valuable information on the reconstruction of a reduced dimensional space based on statistically significant characteristics common to the original data matrix. In other words, these characteristics can be understood as systematic effects present in the light curves, that must be eliminated from the original photometric flux $X^{\rm SAP}$: $X'_{ij} = X_{ij}^{\rm SAP} - X_{ij}^{\rm PCA}$. X' is defined as the matrix containing the light curves after systematics subtraction, where the stellar intrinsic variability is maximized. As a result, light curves that initially showed systematic jumps, after passing through the process of detrending presented a smoother aspect.

Also, the detection limits may be improved by modifying the binning of the light curves, for example, increasing from 2 min cadence to 30 min. Within this time interval, a considerable *TESS* stability would be reached; otherwise, it could introduce errors correlated with the pointing. After that, the amplitude error would reach a distribution close to Poisson, possibly decreasing the baseline limit of detection of the rotational *TESS* amplitudes by a factor of $\sqrt{15}$, or $\sim$3.9.

APPENDIX B: COMPARISON WITH THE LITERATURE

Morris (2020, M20) presented an age photometric amplitude ($A_{\rm M20}$) relation for FGK stars in six associations ranging in ages from 10 Myr to 4 Gyr. The author found $A_{\rm M20} \propto t^{-0.46}$ (see his equation 1) which is very close to the Skumanich-like relation ($\propto t^{-0.5}$). On the other hand, the exponent $n = -1.12$ found in our work indicates a faster decrease in spot contribution until $\approx$3 Gyr, at least. This means that, in relative terms and overevolutionary time-scales, the photometric amplitudes will decrease more rapidly than other activity metrics that are well-known to follow the Skumanich-like trend [as it can be evidenced by equation (6)]. We stress that the methodology and the sample (Kepler space mission) employed in Morris (2020) are different from those presented in this work. Therefore, a word of caution should be taken, when one tries to compare both studies. The apparent disagreement on the age–activity slope may be caused by the different samples adopted. Our sample stars are very close to the solar parameters ($T_{\rm eff} \sim T_{\rm eff,\odot} \pm 100$ K and [Fe/H] $\sim$ [Fe/H]$_\odot \pm 0.1$ dex, see Table 1) unlike those studied by M20 [FGK; $4500 \lesssim T_{\rm eff}$ (K) $\lesssim 6500$], which describes the evolution of solar-type stars in general.

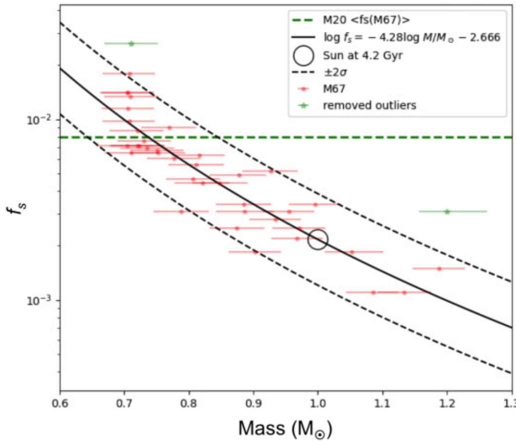

Figure B1. Filling factor as a function of stellar mass (in units of solar mass) for stars in M67, and the Sun (black open circle). The fit to the red points is given by the equation in the box with the $\pm 2\sigma$ shown by the dashed lines. The horizontal dashed green line represents the average result of 0.8 per cent from Morris (2020).

The inclusion of stars over a wide range of $T_{\rm eff}$ tends to blur the age–activity relations owing to their different photospheric properties that increase/decrease the measured photometric amplitude as we consider cooler/hotter stars. To evidence this behaviour, we retrieved $T_{\rm eff}$, log(g), masses and other relevant properties by cross-matching the M20 with *Gaia* DR3 samples. In Fig. B1, we show how the stellar masses are strongly correlated with the photometric amplitudes, or filling factor obtained from using his equation 12 ($\rho = -0.9$, p-value $< 10^{-14}$, $N = 38$). For a given age, low-mass stars show higher photometric amplitudes ranging from 0.02 per cent (M/M$_\odot \sim 1.2$) up to 0.3 per cent (M/M$_\odot \sim 0.7$). To match the solar properties, we fitted a log–log linear regression for M67 data:

$$\log A_{\rm M20}(4.2\ {\rm Gyr}) = -5.784 \log M/{\rm M}_\odot - 1.306 \qquad \text{(B1)}$$

and then, estimated one solar mass photometric variability to be $A_{\rm M20}(4.2\ {\rm Gyr}) = 0.05^{+0.02}_{-0.02}$%. This value corresponds to a photometric filling factor of $0.2^{+0.1}_{-0.2}$ per cent for M67.

Also, this is likely to be the reason why some old Kepler stars strongly deviate from the M20 proposed relation (see his fig. 9). There is a strong tendency to overpopulate the cool $T_{\rm eff}$ domain ($T_{\rm eff} \ll T_{\rm eff,\odot}$) photospheric contrast detection bias is strong, leading to an overpresence of cool stars, which tend to increase the average activity level.

This paper has been typeset from a TEX/LATEX file prepared by the author.